Numerical investigation of electromagnetic wave propagation generated by localized sources using a high order discontinuous Galerkin time domain method

Daniel Gieschen

July 16, 2009

Abstract

This work is concerned with the adaption of an existing high order finite volume method (also referred as discontinuous Galerkin method) for the numerical resolution of the system of two-dimensional Maxwell equations, in order to simulate the propagation of electromagnetic waves generated by localized sources in a complex scene involving different types of obstacles and objects. The numerical method considered in this work assumes that the computational domain is discretized using a triangular mesh and that the electromagnetic field components are approximated using a high order piecewise polynomial interpolation. Further on this work consists of several simulations conducted for different configurations of mesh resolution and approximation order aiming at assessing the numerical accuracy of the adapted discontinuous Galerkin method defined by the numerical treatment of the selected source models in the considered application context which is based on the specification and construction of several triangulations of the propagation scene developped with an appropriate mesh generation tool.

Contents

1 Introduction **3**

2 Theoretical part **4**
2.1 Maxwell equations 4
2.2 Numerical scheme 4
2.2.1 Discontinuous Galerkin time domain method 5
2.3 Source term 6
2.3.1 Delta function 7
2.3.2 Gaussian function 7

3 Numerical study **8**
3.1 Problem statement 8
3.2 Propagation in free space 8
3.2.1 Influence of the discretization step 9
3.2.2 Influence of the interpolation order in the DGTD-$\mathbb{P}_p$ method 12
3.2.3 Influence of the size of the computational domain 15
3.2.4 Analysis of the time evolution of the energy 15
3.3 Propagation involving a room 20
3.3.1 Influence of the electricial permittivity ε and conductivity σ of the wall 20
3.3.2 Influence of the size of the computational domain 23
3.3.3 Influence of the position of the source 23
3.4 Propagation involving objects inside the room 25

4 Conclusions **28**

1 Introduction

Partial differential equations are used to model physical problems involving functions of several variables, such as the propagation of sound or heat, fluid flow, elasticity and electrodynamics. Seemingly distinct physical phenomena may have identical mathematical formulations, and thus be governed by the same underlying dynamics. Electromagnetic wave propagation can be simulated by partial differential equations called the Maxwell equations. In this study the involved physical quantities of these equations are the magnetic and electric fields.

By aiming to solve the Maxwell equations computationally, one notices there are a lot different methods for doing so. For instance there are finite difference, finite element and finite volume methods which derive discrete representations of the spatial derivative operators. After that there are a number of methods to solve the system of ordinary differential equations in time. All of these methods have their advantages but also their drawbacks. A finite difference method cannot handle complex geometries. While a finite volume method (FVM) has geometric flexibility, the main limitation is its difficulty to extend to higher-order accuracy on general unstructed grids. And while a finite element method (FEM) is able to have high-order accuracy on complex geometries it looses the locality of the scheme and fails to have an explicit semi-discrete form. When combining the finite element and finite volume methods in an intelligent way there is the discontinuous Galerkin time domain (DG) method having a variety of advantages to the other schemes. The mass matrix is local, rather than global, and therefore can be inverted at low cost, yielding to an explicit semidiscrete scheme. When designing the numerical flux, there is more flexibility available than in the original FEM. That ensures stability of the wave dominated problems. The DG method achieves a high-order accuracy having a local element-based basis while maintaining local conservation. The main drawback is an increase in the total degrees of freedom.

The overall objective of this study is to develop a numerical methodology that will be used for the design of a radar-based imaging system. We consider several simulation configurations of increasing complexity involving a localized radiating source (emitting antenna) and a set of observation (receiving) antennas. Therefore, in a first part, we begin introducing the theoretical background developping the DG method for the Maxwell equations in two dimensions with a source term. In the main part we investigate numerically the propagation patterns for different scenes.

2 Theoretical part

2.1 Maxwell equations

We shall consider the solution of the two-dimensional Maxwell equations for a z-transverse magnetic (TM) polarization on a bounded domain $\Omega \subset \mathbb{R}^2$:

$$\begin{cases} \varepsilon \dfrac{\partial E_z}{\partial t} - \dfrac{\partial H_y}{\partial x} + \dfrac{\partial H_x}{\partial y} = 0, \\ \mu \dfrac{\partial H_x}{\partial t} + \dfrac{\partial E_z}{\partial y} = 0, \\ \mu \dfrac{\partial H_y}{\partial t} - \dfrac{\partial E_z}{\partial x} = 0, \end{cases} \tag{1}$$

where the magnetic field $\mathbf{H} = {}^t(H_x, H_y, 0)$ is transverse to the z-direction and the electric field $\mathbf{E} = {}^t(0, 0, E_z)$ has only one component along the z-direction. The parameters ε and μ refer to the electric permittivity and magnetic permeability, respectively, of the propagation media. On the boundary $\Gamma = \partial\Omega$ we use either a perfect electric conductor (PEC) condition i.e. $E_z = 0$, or a first order Silver-Müller absorbing boundary condition i.e. $E_z = c\mu(n_y H_x - n_x H_y)$, or both of them, where $c = 1/\sqrt{\varepsilon\mu}$ is the speed of propagation and $\vec{n} = (n_x, n_y)$ denotes the unit normal vector pointing outward to Γ.

2.2 Numerical scheme

We consider a partition $\mathcal{T}_h$ of Ω into a set of triangles T_i of size h_i with boundaries ∂T_i and characteristic mesh size $h = \max_{T_i \in \mathcal{T}_h} h_i$. In general, to each $T_i \in \mathcal{T}_h$ we assign an integer $p_i \geq 0$ (the local interpolation order) and we collect the p_i in the vector $p = \{p_i : T_i \in \mathcal{T}_h\}$. However, in the present study, p_i is uniform in all element T_i of the mesh, so we have $p = p_i$. Each triangle T_i is assumed to be the image, under a smooth bijective (diffeomorphic) mapping τ_i, of a fixed reference triangle $\hat{\mathrm{T}} = \{\hat{x}, \hat{y} |\ \hat{x}, \hat{y} \geq 0; \hat{x} + \hat{y} \leq 1\}$. Assuming that T_i is a straight sided triangle defined through the coordinates of the three vertices $\mathbf{v}_1^i$, $\mathbf{v}_2^i$ and $\mathbf{v}_3^i$ (see Fig. 1), the correspondence between the two triangles $\hat{\mathrm{T}}$ and T_i is established through the use of the barycentric coordinates $(\lambda_1, \lambda_2, \lambda_3)$. We recall that any point $\mathbf{x}^i \in T_i$ can be expressed as a convex combination of the vertices of T_i and the mapping is simply given by $\tau_i : (\hat{x}, \hat{y}) \in \hat{T} \rightarrow \mathbf{x}^i$, such that $\mathbf{x}^i(\hat{x}, \hat{y}) = \lambda_1 \mathbf{v}_1^i + \lambda_2 \mathbf{v}_2^i + \lambda_3 \mathbf{v}_3^i$, where $\lambda_1 + \lambda_2 + \lambda_3 = 1$ and $0 \leq (\lambda_1, \lambda_2, \lambda_3) \leq 1$ with $\lambda_1 = 1 - \hat{x} - \hat{y}$, $\lambda_2 = \hat{x}$ and $\lambda_3 = \hat{y}$.

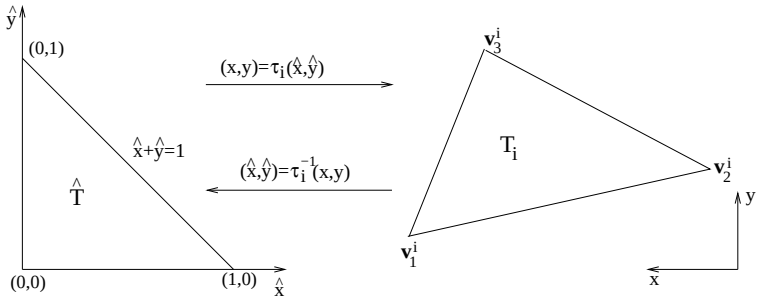

Figure 1: Mapping between the physical triangle T_i and the master triangle $\hat{\mathrm{T}}$.

In the following, for a given partition $\mathcal{T}_h$, we seek for an approximate solution of (1) in the finite dimensional subspace $V_p(\mathcal{T}_h) := \{v \in L^2(\Omega) : v_{|T_i} \in \mathbb{P}_p(T_i)\ ,\ \forall T_i \in \mathcal{T}_h\}$, where $\mathbb{P}_p(T_i)$ denotes the space of nodal polynomials $\{\varphi_{ij}\}_{j=1}^d$ of total degree at most p in the element T_i. The space $V_p(\mathcal{T}_h)$ has the dimension d, the local number of degrees of freedom. Note that a function $v_h^p \in V_p(\mathcal{T}_h)$ might be discontinuous across element interfaces. For each triangle T_i, ε_i and μ_i respectively denote the local constant electric permittivity and magnetic permeability. For two neighboring triangles T_i and T_k in $\mathcal{T}_h$, the (non-empty) intersection $T_i \cap T_k$ is an (oriented) edge s_{ik} which we will call *interface*, with oriented normal vector $\vec{n}_{ik}$ and with unitary one $\vec{\tilde{n}}_{ik}$. For the boundary interfaces, the index k corresponds to

a fictitious element outside the domain. Finally, we denote by $\mathcal{V}_i$ the set of indices of the neighbors elements of T_i.

2.2.1 Discontinuous Galerkin time domain method

We now derive the spatial discretization. Taking the product of system (1) by a given basis function $\varphi_{ij} \in \mathbb{P}_p(T_i), 1 \leq j \leq d$, and integrating over T_i yields :

$$\left\{ \begin{array}{lcll} \displaystyle\int_{T_i} \varepsilon_i \frac{\partial E_z}{\partial t}\varphi_{ij} & + & \displaystyle\int_{T_i} H_y \frac{\partial \varphi_{ij}}{\partial x} - \int_{T_i} H_x \frac{\partial \varphi_{ij}}{\partial y} & \\ & - & \displaystyle\int_{\partial T_i} H_y \varphi_{ij} \widetilde{n}_{ikx} + \int_{\partial T_i} H_x \varphi_{ij} \widetilde{n}_{iky} & = 0, \\ \displaystyle\int_{T_i} \mu_i \frac{\partial H_x}{\partial t}\varphi_{ij} & - & \displaystyle\int_{T_i} E_z \frac{\partial \varphi_{ij}}{\partial y} + \int_{\partial T_i} E_z \varphi_{ij} \widetilde{n}_{iky} & = 0, \\ \displaystyle\int_{T_i} \mu_i \frac{\partial H_y}{\partial t}\varphi_{ij} & + & \displaystyle\int_{T_i} E_z \frac{\partial \varphi_{ij}}{\partial y} - \int_{\partial T_i} E_z \varphi_{ij} \widetilde{n}_{ikx} & = 0. \end{array} \right. \tag{2}$$

For any field $\mathrm{X} \in \{E_z, H_x, H_y\}$, we denote by X_i the L^2-projection on the linear space $\mathsf{Span}\{\varphi_{ij},\ 1 \leq j \leq d\}$ spanned by functions defined on T_i, and where $\{\varphi_{ij}\}_{j=1,\ldots,d} \in \mathbb{P}_p(T_i)$ is a family of linearly independent functions. In each triangle T_i we construct a polynomial representation of the magnetic and electric fields and for simplicity and efficiency reasons we adopt a Lagrangian interpolation approach based on a set of nodes defined on the master (reference) triangle $\hat{\mathrm{T}}$. Using this notation, we have the following global discontinuous representation of the field:

$$\mathrm{X} \simeq \sum_i \mathrm{X}_i(t,x,y) = \sum_i \sum_{j=1}^{d} X_{ij}(t)\varphi_{ij}(x,y), \tag{3}$$

where X_{ij} is the jth degree of freedom of the field X_i. We denote by $\mathbf{X}_i$ the column vector $(X_{ij})_{1\leq j\leq d}$. The approximation field $\mathrm{X}_h \in \{(E_z)_h, (H_x)_h, (H_y)_h\}$, defined by $(\mathrm{X}_{h|T_i} = \mathrm{X}_i, \forall i)$ is allowed to be discontinuous across element boundaries and, for such a discontinuous field X_h, we define its average $\{\mathrm{X}_h\}_{ik}$ on any internal face s_{ik}, as:

$$\{\mathrm{X}_h\}_{ik} = \frac{\mathrm{X}_{i|s_{ik}} + \mathrm{X}_{k|s_{ik}}}{2}. \tag{4}$$

Note that for any internal face s_{ik}, $\{\mathrm{X}_h\}_{ik} = \{\mathrm{X}_h\}_{ki}$. For any integral over ∂T_i, a specific treatment must be introduced since the approximate fields are discontinuous through element faces. We choose to use a centered approximation:

$$\forall i, \forall k \in \mathcal{V}_i,\ \mathrm{X}_{|s_{ik}} \simeq \{\mathrm{X}_h\}_{ik}. \tag{5}$$

For what concerns time discretization, we propose to use a leap-frog time integration scheme which has both the advantage to be explicit and free of time dissipation. In the sequel, superscripts refer to time stations and Δt is the fixed time-step. The unknowns related to the electric field are approximated at integer time stations $t^n = n\Delta t$ and are denoted by $\mathbf{E}^n_{z_i}$. The unknowns related to the magnetic field are approximated at half-integer time stations $t^{n+\frac{1}{2}} = (n+\frac{1}{2})\Delta t$ and are denoted by $\mathbf{H}^{n+\frac{1}{2}}_{x_i}$ and $\mathbf{H}^{n+\frac{1}{2}}_{y_i}$.

The boundary conditions on Γ are treated in a weak sense by defining some values for the fields E_z, H_x and H_y in the fictitious neighboring element T_k. The treatment of boundary conditions is weak in the sense that the traces on $s_{ik} \in \Gamma$ of fictitious fields $\mathbf{E}^n_{z_k}, \mathbf{H}^{n+\frac{1}{2}}_{x_k}$ and $\mathbf{H}^{n+\frac{1}{2}}_{y_k}$ are used for the computation of numerical fluxes for the boundary element T_i. More precisely, for a metallic boundary interface s_{ik}, the fictitious values are chosen as :

$$\forall (x,y) \in s_{ik} : \left\{ \begin{array}{l} \mathbf{H}^{n+\frac{1}{2}}_{x_k}(x,y) = \mathbf{H}^{n+\frac{1}{2}}_{x_i}(x,y), \quad \mathbf{H}^{n+\frac{1}{2}}_{y_k}(x,y) = \mathbf{H}^{n+\frac{1}{2}}_{y_i}(x,y), \\ \mathbf{E}^n_{z_k}(x,y) = -\mathbf{E}^n_{z_i}(x,y), \end{array} \right. \tag{6}$$

and for an absorbing boundary interface s_{ik}, the fictitious values are :

$$\forall (x,y) \in s_{ik} : \ \mathbf{E}_{z_k}^{n+1}(x,y) = c_i \mu_i (n_{iky} \mathbf{H}_{x_i}^{n+\frac{1}{2}}(x,y) - n_{ikx} \mathbf{H}_{y_i}^{n+\frac{1}{2}}(x,y)). \tag{7}$$

The discontinuous Galerkin DGTD-$\mathbb{P}_p$ method can be written in the following matrix form:

$$\left\{ \begin{array}{rcl} \mathbb{M}_i^{\varepsilon} \dfrac{\mathbf{E}_{z_i}^{n+1} - \mathbf{E}_{z_i}^{n}}{\Delta t} & = & -\mathbb{K}_i^x \mathbf{H}_{y_i}^{n+\frac{1}{2}} + \mathbb{K}_i^y \mathbf{H}_{x_i}^{n+\frac{1}{2}} \\ & & + \displaystyle\sum_{k \in \mathcal{V}_i} \big(\mathbb{G}_{x_{ik}}^{n+\frac{1}{2}} - \mathbb{G}_{y_{ik}}^{n+\frac{1}{2}} \big), \\ \mathbb{M}_i^{\mu} \dfrac{\mathbf{H}_{x_i}^{n+\frac{1}{2}} - \mathbf{H}_{x_i}^{n-\frac{1}{2}}}{\Delta t} & = & \mathbb{K}_i^y \mathbf{E}_{z_i}^{n} - \displaystyle\sum_{k \in \mathcal{V}_i} \mathbb{F}_{y_{ik}}^{n}, \\ \mathbb{M}_i^{\mu} \dfrac{\mathbf{H}_{y_i}^{n+\frac{1}{2}} - \mathbf{H}_{y_i}^{n-\frac{1}{2}}}{\Delta t} & = & -\mathbb{K}_i^x \mathbf{E}_{z_i}^{n} + \displaystyle\sum_{k \in \mathcal{V}_i} \mathbb{F}_{x_{ik}}^{n}, \end{array} \right. \tag{8}$$

where the vector quantities $\mathbb{F}_{xik}^n, \mathbb{F}_{yik}^n, \mathbb{G}_{xik}^{n+\frac{1}{2}}$ and $\mathbb{G}_{yik}^{n+\frac{1}{2}}$ are defined as:

$$\left\{ \begin{array}{lll} \mathbb{F}_{x_{ik}}^n = \mathbb{S}_{ik}^x \mathbf{E}_{z_k}^n & , & \mathbb{F}_{y_{ik}}^n = \mathbb{S}_{ik}^y \mathbf{E}_{z_k}^n, \\ \mathbb{G}_{x_{ik}}^{n+\frac{1}{2}} = \mathbb{S}_{ik}^x \mathbf{H}_{y_k}^{n+\frac{1}{2}} & , & \mathbb{G}_{y_{ik}}^{n+\frac{1}{2}} = \mathbb{S}_{ik}^y \mathbf{H}_{x_k}^{n+\frac{1}{2}}, \end{array} \right. \tag{9}$$

and the positive definite symmetric mass matrices $\mathbb{M}_i^{\varepsilon}$, $\mathbb{M}_i^{\mu}$, and the skew-symmetric stiffness matrix $\mathbb{K}_i^{\mathbf{x}}$, $\mathbf{x} \in \{x, y\}$ (all of size $d_i \times d_i$) are given by:

$$\left\{ \begin{array}{l} (\mathbb{M}_i^{\varepsilon})_{jl} = \displaystyle\int_{T_i} \epsilon_i \varphi_{ij} \varphi_{il}, \quad (\mathbb{M}_i^{\mu})_{jl} = \int_{T_i} \mu_i \varphi_{ij} \varphi_{il}, \\ (\mathbb{K}_i^{\mathbf{x}})_{jl} = \dfrac{1}{2} \displaystyle\int_{T_i} \Big(\frac{\partial \varphi_{ij}}{\partial \mathbf{x}} \varphi_{il} - \varphi_{ij} \frac{\partial \varphi_{il}}{\partial \mathbf{x}} \Big). \end{array} \right. \tag{10}$$

For any interface s_{ik}, the $d_i \times d_k$ rectangular interface matrix $\mathbb{S}_{ik}^{\mathbf{x}}$, $\mathbf{x} \in \{x, y\}$ is given by:

$$(\mathbb{S}_{ik}^{\mathbf{x}})_{jl} = \frac{1}{2} \widetilde{n}_{ik\mathbf{x}} \int_{s_{ik}} \varphi_{ij} \varphi_{kl}. \tag{11}$$

For any interface matrix $\mathbb{S}_{ik}^{\mathbf{x}}$, we have the following properties:

- if s_{ik} is an internal interface of the mesh then ${}^t\mathbb{S}_{ik}^{\mathbf{x}} = -\mathbb{S}_{ki}^{\mathbf{x}}$,
- if s_{ik} is a metallic boundary interface of the mesh then ${}^t\mathbb{S}_{ik}^{\mathbf{x}} = \mathbb{S}_{ik}^{\mathbf{x}}$.

For energy analysis we define the discrete electromagnetic energy:

$$\mathcal{E}^n = \frac{1}{2} \sum_i ({}^t\mathbf{E}_{z_i}^n \mathbb{M}_i^{\varepsilon} \mathbf{E}_{z_i}^n + {}^t\mathbf{H}_{x_i}^{n-\frac{1}{2}} \mathbb{M}_i^{\mu} \mathbf{H}_{x_i}^{n+\frac{1}{2}} + {}^t\mathbf{H}_{y_i}^{n-\frac{1}{2}} \mathbb{M}_i^{\mu} \mathbf{H}_{y_i}^{n+\frac{1}{2}}). \tag{12}$$

The convergence order in apce and time is:

$$\mathcal{O}(Th^{\min(s,p)}) + \mathcal{O}(\Delta t^2). \tag{13}$$

2.3 Source term

So far, we have presented a numerical scheme to solve the source free Maxwell equations. For the propagation problems considered in the present study, we have to take into account a source terme corresponding to a current field generated by a localized source. More precisely, we consider a source term along the z-direction $\mathbf{J} = {}^t(0, 0, J_z)$:

$$\varepsilon \frac{\partial E_z}{\partial t} - \frac{\partial H_y}{\partial x} + \frac{\partial H_x}{\partial y} = -J_z(x, y, t), \tag{14}$$

where the current $J_z(x, y, t)$ can take one of the two forms discussed below.

2.3.1 Delta function

The source term writes $J_z(x,y,t) = f(t)\delta(x-x_0, y-y_0)$ where $f(t)$ is a given function in time and:

$$\delta(x-x_0, y-y_0) = \begin{cases} 1 & \text{if } x = x_0,\ y = y_0, \\ 0 & \text{elsewhere.} \end{cases} \tag{15}$$

For the spatial discretization, integrating (14) over T_i with a given basis function $\varphi_{ij} \in \mathbb{P}_p(T_i)$, we obtain:

$$-\int_{T_i} \varepsilon_i \frac{\partial E_z}{\partial t}\varphi_{ij} + \int_{T_i} H_y \frac{\partial \varphi_{ij}}{\partial x} - \int_{T_i} H_x \frac{\partial \varphi_{ij}}{\partial y} - \int_{\partial T_i} H_y \varphi_{ij} \widetilde{n}_{ikx} + \int_{\partial T_i} H_x \varphi_{ij} \widetilde{n}_{iky} = -\int_{T_i} J_z \varphi_{ij}, \tag{16}$$

and with the properties of the Dirac Delta function we find that:

$$\int_{T_i} J_z \varphi_{ij} = f(t) \int_{T_i} \delta(x-x_0, y-y_0)\varphi_{ij} = f(t)\varphi_{ij}(x_0, y_0). \tag{17}$$

The discrete equation for E_z becomes:

$$\mathbb{M}_i^{\varepsilon} \frac{\mathbf{E}_{z_i}^{n+1} - \mathbf{E}_{z_i}^{n}}{\Delta t} = -\mathbb{K}_i^x \mathbf{H}_{y_i}^{n+\frac{1}{2}} + \mathbb{K}_i^y \mathbf{H}_{x_i}^{n+\frac{1}{2}} + \sum_{k \in \mathcal{V}_i} \left(\mathbb{G}_{x_{ik}}^{n+\frac{1}{2}} - \mathbb{G}_{y_{ik}}^{n+\frac{1}{2}} \right) - f(t)\varphi_{ij}(x_0, y_0). \tag{18}$$

Then, the numerical treatement of a source term of this type is such that the right-hand side in (18) is non-zero only for the degrees of freedom of the element $T \in \mathcal{T}_h$ enclosing the point (x_0, y_0).

2.3.2 Gaussian function

In this case, the source term writes $J_z(x,y,t) = f(t)g(x,y)$ where g is defined by:

$$g(x,y) = Ae^{-\left((x-x_o)^2 + (y-y_o)^2\right)} \tag{19}$$

where A is the amplitude. For the spatial discretization, integrating (14) over T_i with a given basis function $\varphi_{ij} \in \mathbb{P}_p(T_i)$, we obtain:

$$\int_{T_i} J_z \varphi_{ij} = f(t) \int_{T_i} \sum_j g(x_j, y_j)\varphi_{ij}(x,y), \tag{20}$$

which leads to:

$$\mathbb{M}_i^{\varepsilon} \frac{\mathbf{E}_{z_i}^{n+1} - \mathbf{E}_{z_i}^{n}}{\Delta t} = -\mathbb{K}_i^x \mathbf{H}_{y_i}^{n+\frac{1}{2}} + \mathbb{K}_i^y \mathbf{H}_{x_i}^{n+\frac{1}{2}} + \sum_{k \in \mathcal{V}_i} \left(\mathbb{G}_{x_{ik}}^{n+\frac{1}{2}} - \mathbb{G}_{y_{ik}}^{n+\frac{1}{2}} \right) - \mathbb{M}_i \mathbf{G}_{z_i}^{n}, \tag{21}$$

where the discretized source term $\mathbf{G}_{z_i}^n$ and the positive definite symmetric mass matrix $\mathbb{M}_i$ are defined by:

$$\begin{cases} (\mathbb{M}_i)_{jl} &= \displaystyle\int_{T_i} \varphi_{ij}\varphi_{il}, \\ \mathbf{G}_{z_i}^n &= \displaystyle\sum_j g(x_j - x_0, y_j - y_0) \end{cases} \tag{22}$$

Then, the numerical treatement of a source term of this type is such that the right-hand side in (21) is non-zero for the degrees of freedom of the elements $T \in \mathcal{T}_h$ belonging to the support of the Gaussian function.

3 Numerical study

3.1 Problem statement

The overall objective of this study is to develop a numerical methodology that will be used for the design of a radar-based imaging system. We consider several simulation configurations of increasing complexity involving a localized radiating source (emitting antenna) and a set of observation (receiving) antennas. The objective is to record the propagation patterns for different scenes involving a room and objects within the room. In a complementary study, signal processing tools are developed for anlyzing the transmitted/reflected signals. The temporal variation $f(t)$ of the source terms considered in this study is shown on Fig. 2.

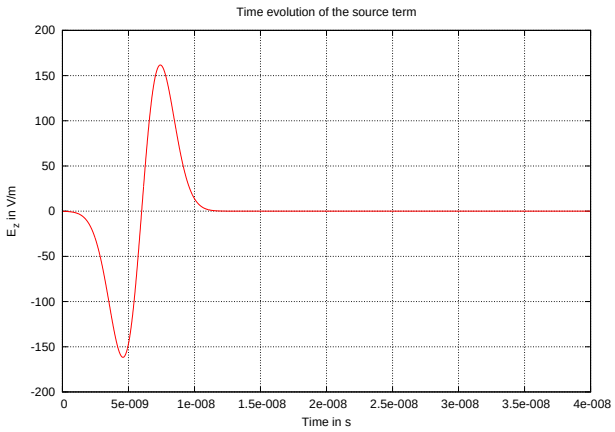

Figure 2: Temporal variation $f(t)$ of the source term.

In theory, the problems that we have to consider are defined in an unbounded space. In practice, the computational domain is truncated artificially and a first order Silver-Müller absorbing boundary condition, $E_z = c\mu(n_y H_x - n_x H_y)$, is imposed on the associated artificial boundary. Therefore, a first series of numerical experiments aim at assessing numerically the accuracy of this approximation and in particular, if artificial reflections appear that pollute the numerical solution. For that purpose, we consider three parameters that may influence the discretization process: the position of the artificial boundary, the discretization step (i.e. the parameter h) and the interpolation order (i.e. the parameter p in the DGTD-$\mathbb{P}_p$ method). So the investigating procedure is to pick one of the above variables, fix the others and analyse the numerical solution in terms of reflection and convergence. For the analysis of reflection we mainly use the Dirac type source and for the analysis of the numerical convergence of the solution we also consider the Gaussian type source. In a second series of numerical experiments the above mentioned scenes involving a room and objects within the room are implemented for exemplary settings and analysed for the following parameters: the electricial permittivity and coductivity (i.e. the parameters ε and σ), the position of the artificial boundary, the position of the radiating source and the type of object within the room (i.e. either a metallic object or an meshed object having a specific ε and σ).

3.2 Propagation in free space

The simulation setting is shown in Fig. 3. The radiating source is located at the center of the domain and the signal is observed at two visualization points. For this series of numerical experiments, the triangular meshes are uniform and deduced from a finite difference grid with $N \times N$ points (i.e with N discretization points along the x- and y-axis). Each square element of this finite difference grid yields two identical triangles.

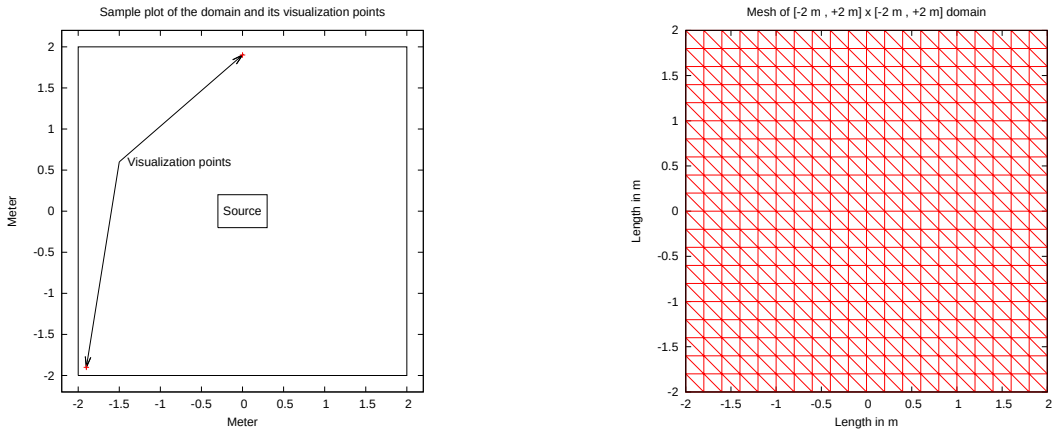

Figure 3: Problem setting for propagation in free space

3.2.1 Influence of the discretization step

We first investigate the influence of the discretization parameter h. Given the size of the square domain (see Fig. 3) in terms of the length L of its sides, the discretization parameter h can be related to the ratio L/N. We have considered the following configurations:

$$L = \begin{cases} 1\,m & \text{if } \Omega = [-0.5\ m, +0.5\ m]^2, \\ 2\,m & \text{if } \Omega = [-1\ m, +1\ m]^2, \\ 4\,m & \text{if } \Omega = [-2\ m, +2\ m]^2, \end{cases} \tag{23}$$

and four uniform triangular meshes referred as:

- `Small` with $N = 6$,
- `Medium` with $N = 11$,
- `High` with $N = 21$,
- `Very High` with $N = 41$.

Generally we will expect that the mesh resolution will have an emphasizing effect if there is a reflection. The finer the mesh the more accurate the solution should be. A possible reflection should be more visible when using a finer mesh.

In the plots of Fig. 4 and Fig. 5 we see a very similar picture at both visualization points. Of course the mesh resolution increases when the size of the computational domain decreases. So when looking at the subplots we should take in account that the mesh resolution is dependent on the dimension of the size of the computational domain which can be seen in Tab. 1. The highlighted figures are an example of a comparable setting.

Number of discretization points N		**6**	**11**	**21**	**41**
Size of the computational domain L	**1 m**	6	**11**	21	41
	2 m	3	5.5	**10.5**	20.5
	4 m	1.5	2.75	5.25	**10.25**

Table 1: Mesh resolution in $^{\#points}/_{meter}$

In general we do not see any reflection on these plots. In fact for the smaller domains the mesh resolution has not even an effect on the first two peaks. The only plots where we can see a development due to the mesh resolution are the corresponding to the largest computational domain ($L = 4\,m$). We can see that the peaks have a lower amplitude with a small resolution than with a higher one, so the

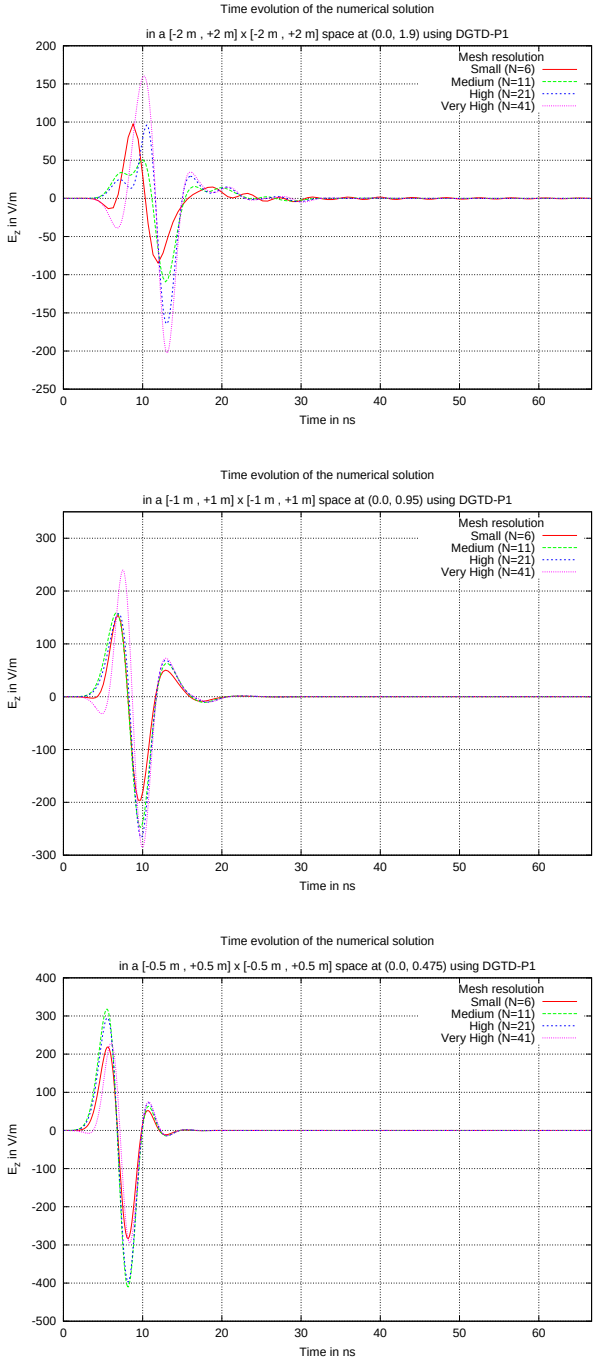

Figure 4: Time evolution for the numerical solution at the top center visualization point (Dirac source type)

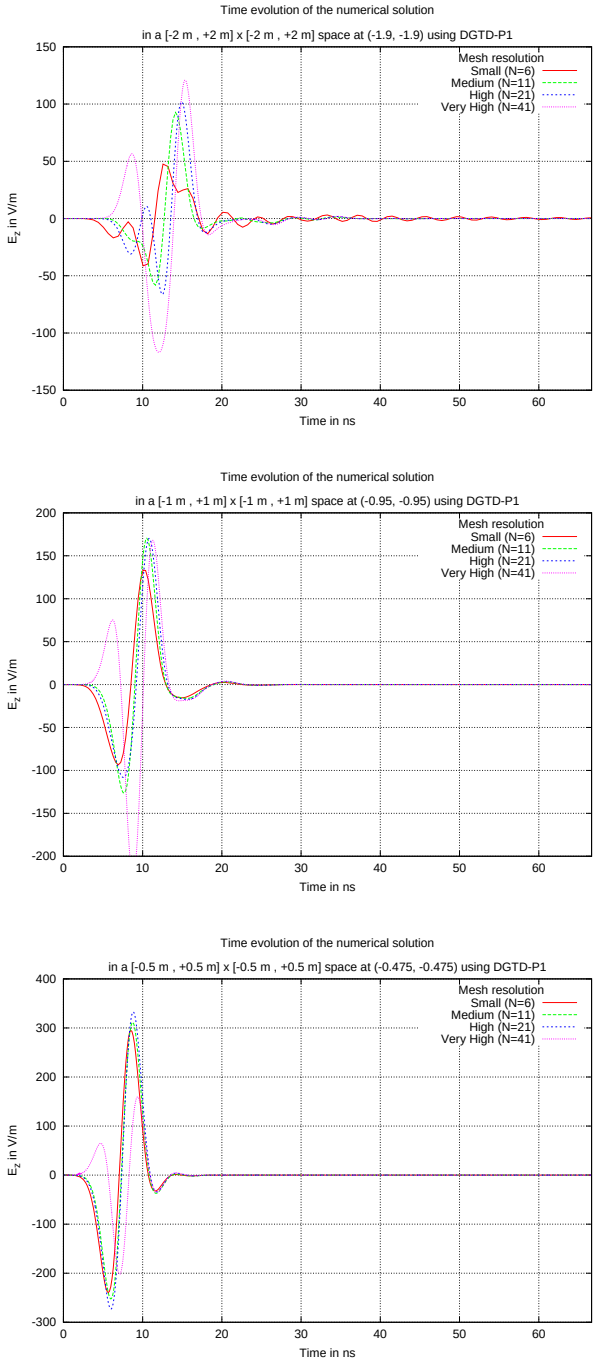

Figure 5: Time evolution for the numerical solution at the bottom left visualization point (Dirac source type)

emphasizing effect is observed. But in any case, although it seems that there might be a reflection looking at the small mesh resolution in the large domain this is not confirmed observing the higher mesh resolutions. In the next plots (Fig. 6 and Fig. 7) we look at the particular case of a large domain ($L = 4\ m$) and zoom in the end of the simulation time window. These plots show more precisely the influence of the mesh resolution on the artificial reflections at the absorbing boundary. We observe that for a low resolution (mesh `Small`), the amplitude of the reflection is about 1% at $t = 50$ and further decreases with the simulation time.

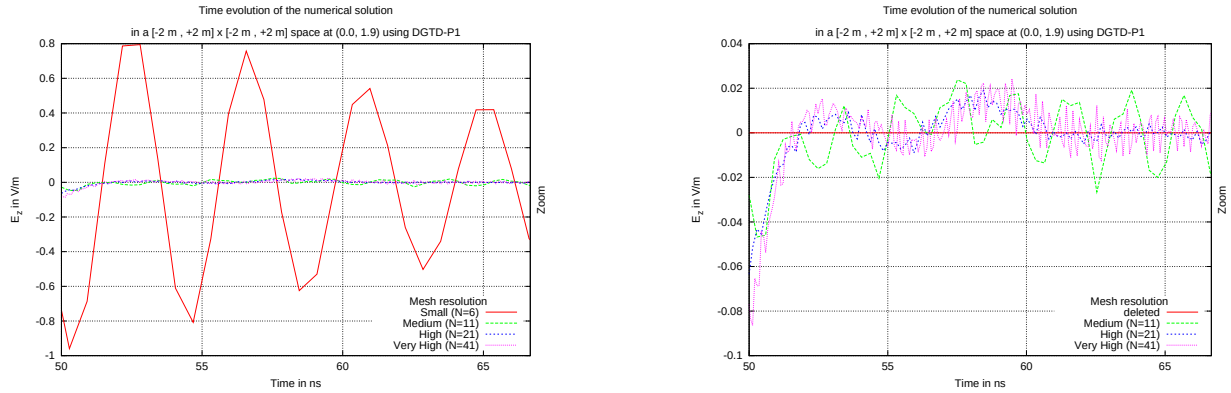

Figure 6: Time evolution for the numerical solution at the top center visualization points with zoom (Dirac source type)

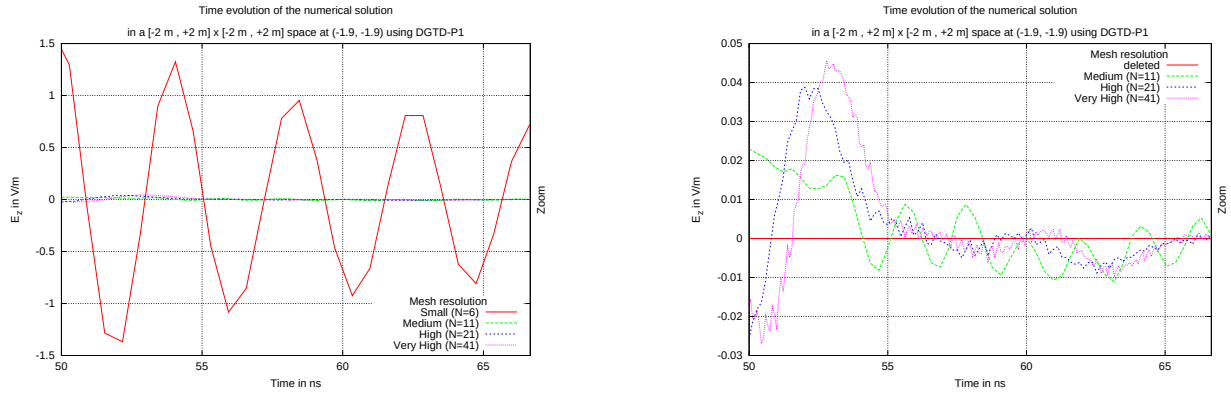

Figure 7: Time evolution for the numerical solution at the bottom left visualization point with zoom (Dirac source type)

3.2.2 Influence of the interpolation order in the DGTD-$\mathbb{P}_p$ method

We now analyze the influence of the interpolation order p in the DGTD-$\mathbb{P}_p$ method. The expectation is that the numerical solutions increase accuracy when the interpolation order is increased.

In the plots of Fig. 8 we again do not see any reflection at the absorbing boundary. In order to observe the accuracy of the numerical solution we compare the soulutions for the different source types (see Fig. 9). For the Gaussian source type, we investigate the convergence of the solution. This means, that for $p = 1$ the DGTD-$\mathbb{P}_p$ method tends to have larger amplitudes in absolute values than for $p > 1$. After that the plots for $p = 2, 3, 4$ seem to converge. Comparing the Gaussian and Dirac source types we

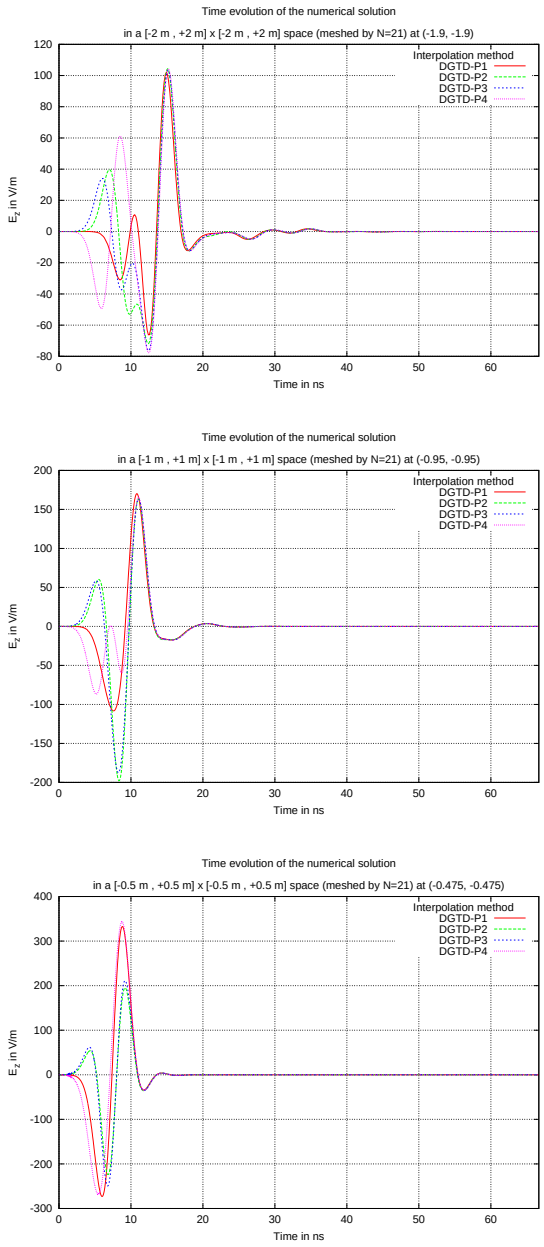

Figure 8: Time evolution for the numerical solution in terms of interpolation order (Dirac source type)

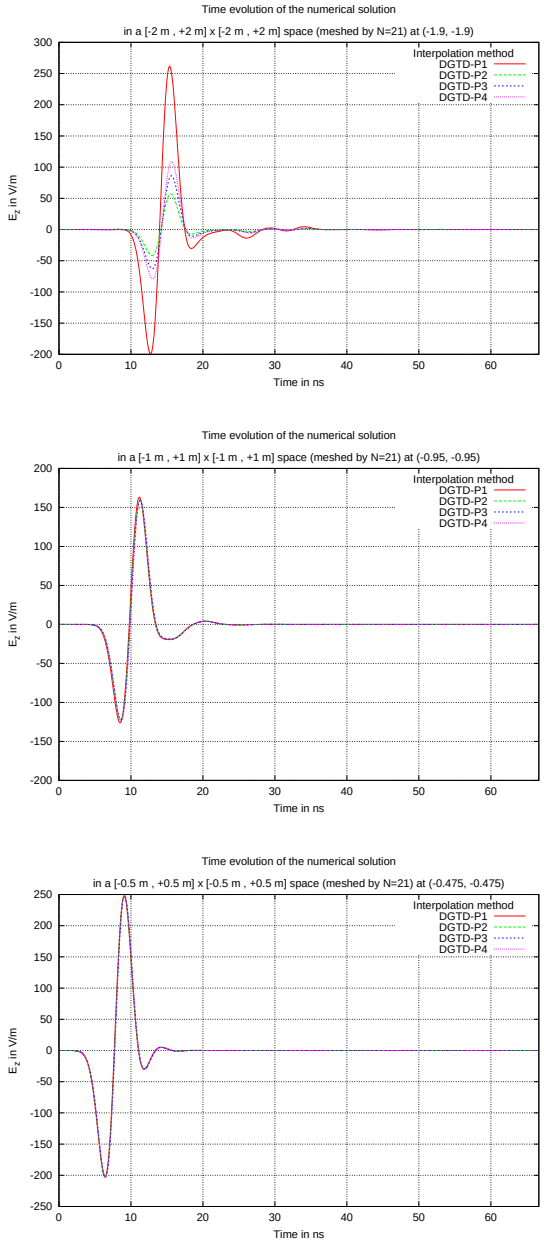

Figure 9: Time evolution for the numerical solution in terms of interpolation order (Gaussian source type)

see as well a convergence, but only towards the second peak. The first peak of the the Dirac source type does not converge. For the larger computational domains we can observe that for the Dirac source type we have basically the same solution for any order of the DGTD-$\mathbb{P}_p$ method. For the Gaussian source type, the solutions of the different orders seem to coincide totally for the smaller domains. We can conclude that a higher order of the DGTD-$\mathbb{P}_p$ method leads to a more accurate solution.

3.2.3 Influence of the size of the computational domain

Here we analyze the influence of the size of the computational domain on the time evolution of the numerical solution. All the simulations reported here have been performed using the DGTD-$\mathbb{P}_2$ method. On the plots of Fig. 10 we see that there is time shift and different absolute values of the amplitudes for both source types. We observe for the first time that the Dirac source type seems to be more consistent than the Gaussian source type source. When zooming (see Fig. 11) we see that the Gaussian source type is smoother towards the end of the simulation. We also observe that for a comparable mesh resolution we have a lot more noise (higher amplitude) in the larger domain than in the smaller ones.

3.2.4 Analysis of the time evolution of the energy

We finally analyze the time evolution of the discrete energy of the whole system. We expect that in all cases the energy of the system converges to zero very quickly since we have not observed any reflections at the abosrbing boundary.

From the plots of Fig. 12 we see that in a smaller domain we have a faster convergence of the energy of the system for the case of a Dirac source type. We also observe that for the Dirac source type the energy converges the fastest for the DGTD-$\mathbb{P}_2$ method. The plots of Fig. 13 confirm that for a smaller domain there is a faster convergence as well as for the higher mesh resolution. But although we sometimes confirm that with a higher DGTD-$\mathbb{P}_p$ method the energy converges faster, we also see that the plots for $p = 2$ and $p = 3$ change so that the DGTD-$\mathbb{P}_2$ method converges faster than the DGTD-$\mathbb{P}_3$ method. Comparing Fig. 12 and Fig. 13 we see that the energy converges faster in the case of a Gaussian source type than in the case of Dirac source type.

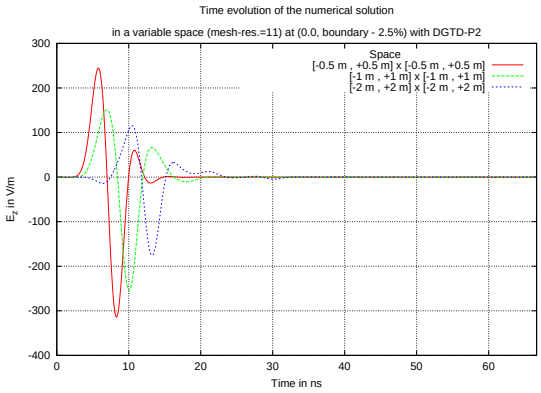

(a) Dirac source type

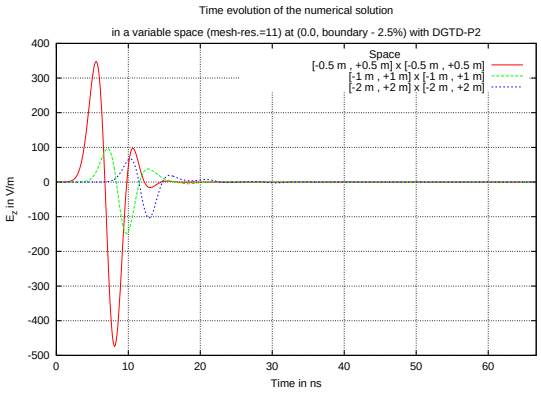

(b) Gaussian source type

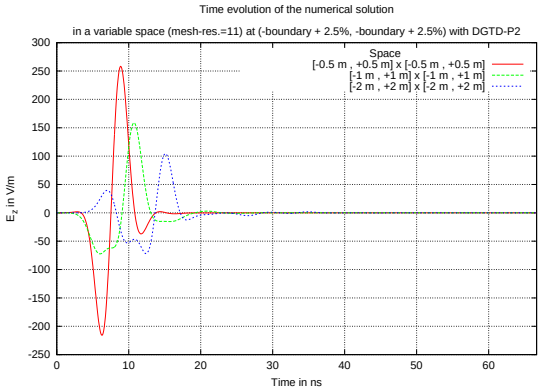

(c) Dirac source type

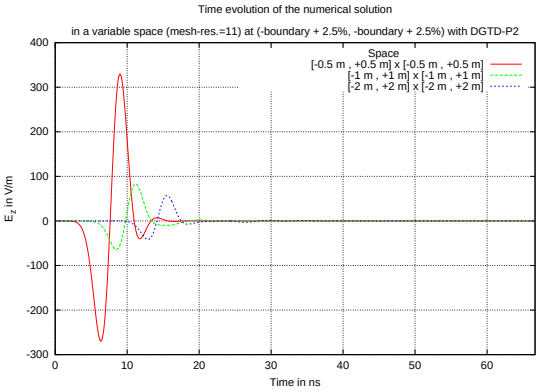

(d) Gaussian source type

Figure 10: Time evolution for the numerical solution at both visualization points in terms of size of the domain

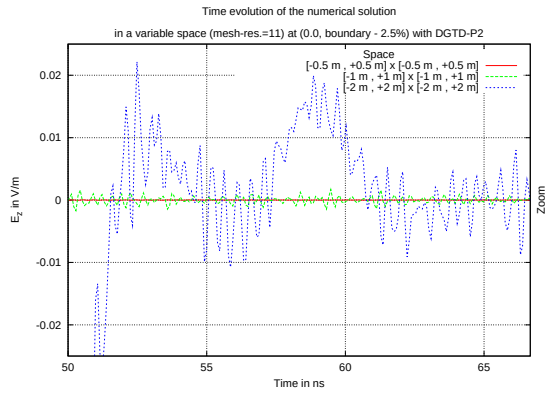

(a) Dirac source type

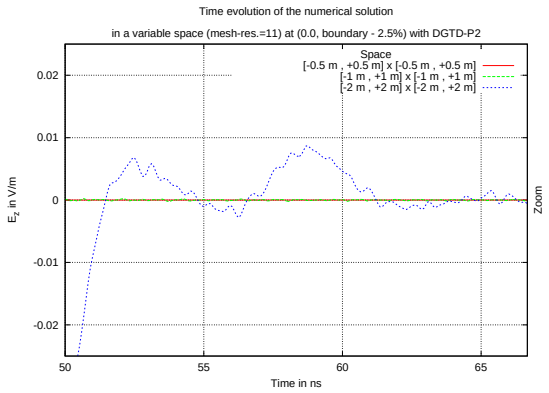

(b) Gaussian source type

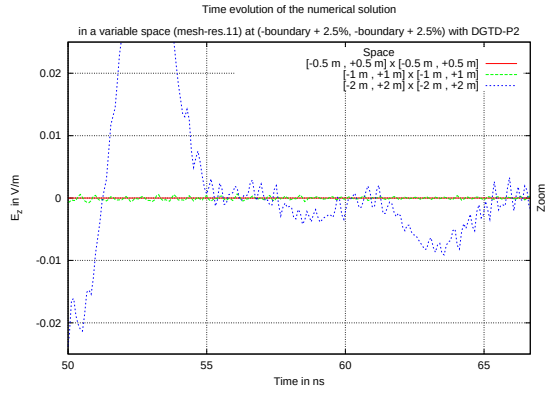

(c) Dirac source type

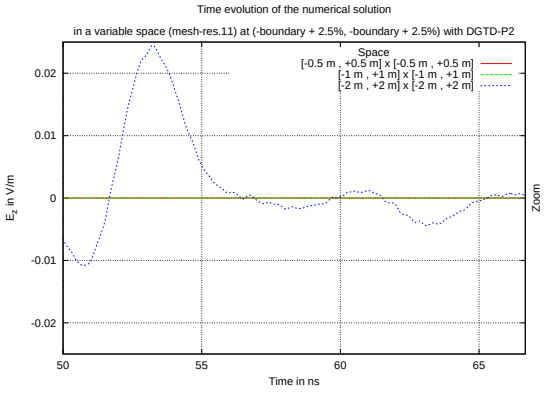

(d) Gaussian source type

Figure 11: Time evolution for the numerical solution at both visualization points in terms of size of the domain (zoom)

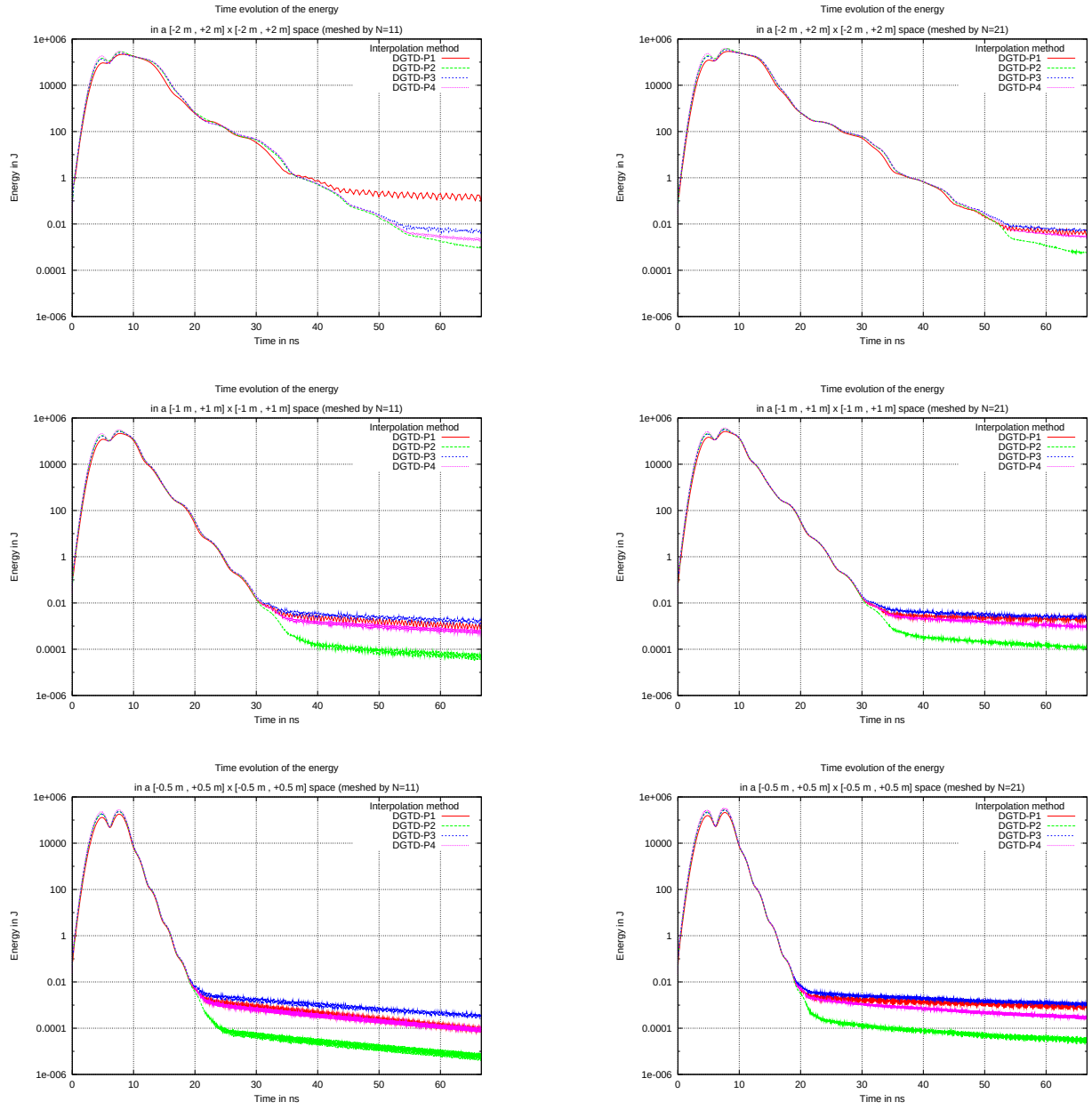

Figure 12: Time evolution for the discrete energy in terms of the interpolation order in log scale (Dirac source type)

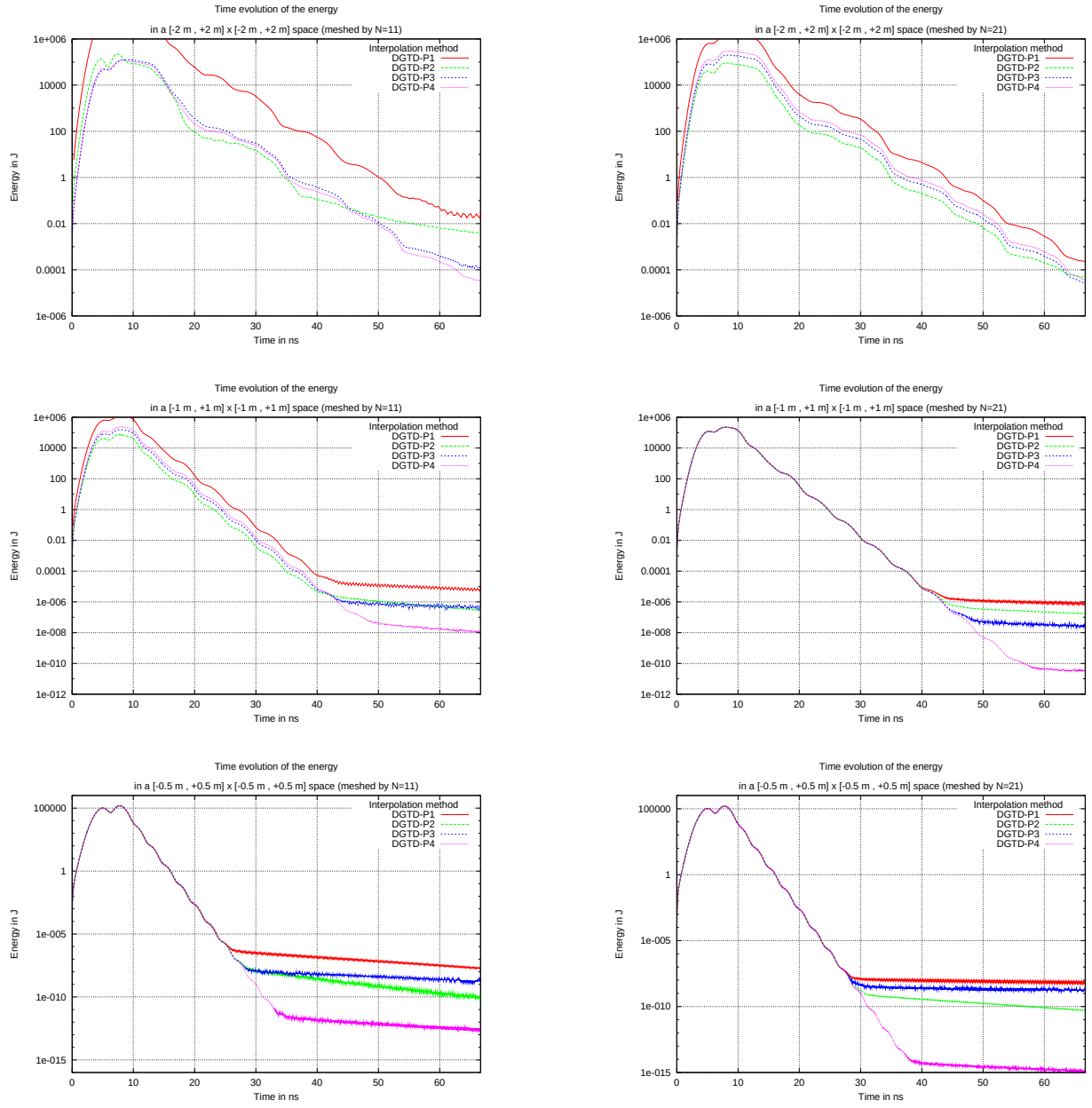

Figure 13: Time evolution for the energy in terms of the interpolation ordre in log scale (Gaussian source type)

3.3 Propagation involving a room

The meshes of the simulation settings are shown on Fig. 14. The radiating source is still located at the center of the domain. For this series of numerical experiments, the triangular meshes are generated with the FreeFem software. A square room is modeled inside the domain having walls of $20\,cm$ depth. Unlike the first series of numerical experiments the data plotted in each figure exclusivly refers to the interpolation order p in the DGTD-$\mathbb{P}_p$ method for $p \in \{1, 2, 3, 4\}$.

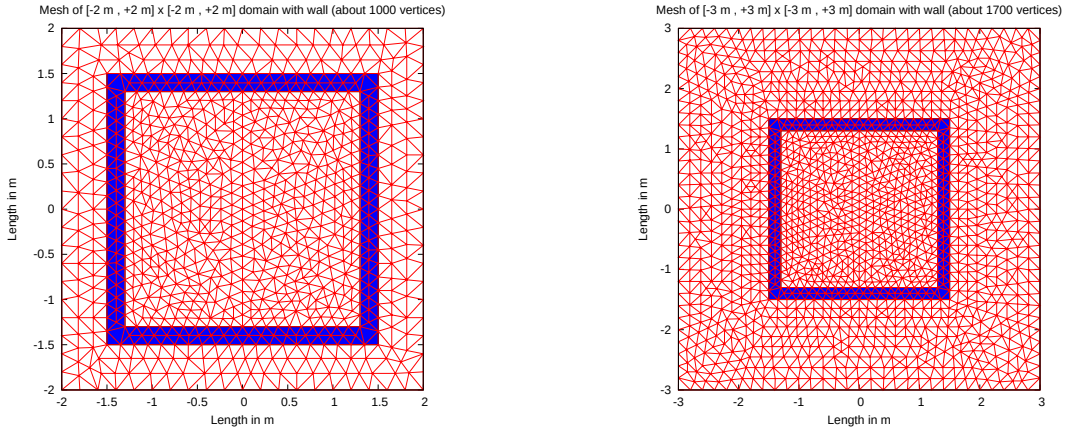

Figure 14: Problem setting for propagation involving a room

3.3.1 Influence of the electricial permittivity ε and conductivity σ of the wall

In this section we analyse the change of the signal, observed at the same visualization point outside of the room, when the physical properties of the walls change. The values for the electricial permittivity ε and the conductivity σ are chosen arbitrarily and may not coincide with the real physical values of a wall. We expect for an increase of ε that a reflection at the wall occurs so that the measured electric field $\mathbf{E}$ will have lower amplitudes and the discrete energy of the system will last longer inside the room. When increasing the conductivity we expect the discrete energy to decrease.

The plots in Fig. 15 and Fig. 16 show the observed signal for different values of ε and σ and the discrete energy of the system in those cases. We see for both source types there are very similar plots. As well we observe that there is a convergence when increasing the DGTD-$\mathbb{P}_p$ method. These patterns are due to a high resoluted mesh, based on about 1000 points in a $[-2\,m, +2\,m]^2$ domain. When analysing further on we use the Dirac source type only, knowing that exceptional plots of the lowest interpolation order might occur. By exceptional plots we mean the plots of interpolation order $p = 1$ for the DGTD-$\mathbb{P}_p$ method in Fig. 15 and Fig. 16 for the Dirac source type (i.e. the red-colored lines).

We in fact observe reflecting patterns when increasing the permittivity, so that the amplitudes of the electric field decrease but the number of peaks increase during the investigation. Also the discrete energy remains longer in the system than for the free space setting. It is about 0.1% at $t = 100$ (instead of 0.00001% at $t = 50$). We also observe a decreasing discrete energy when the conductivity is increased. Moreover the amplitude of the electric field decreases as well.

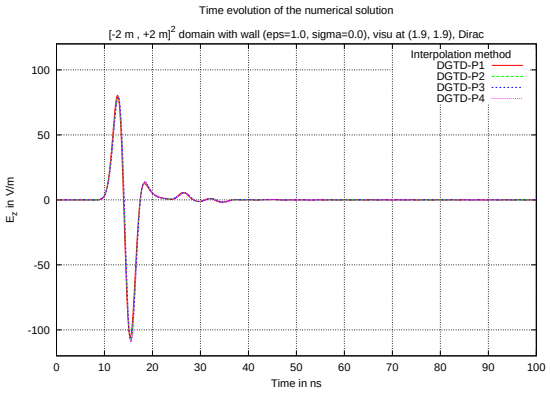

(a) Dirac source type

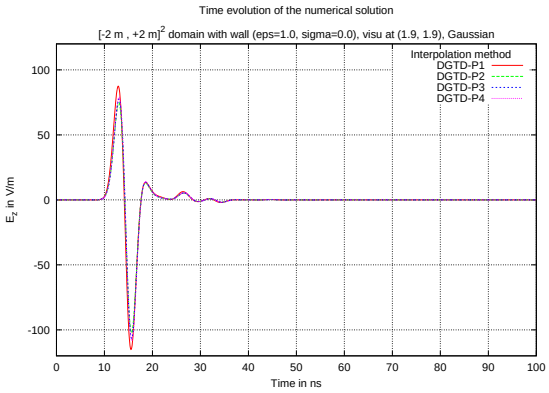

(b) Gaussian source type

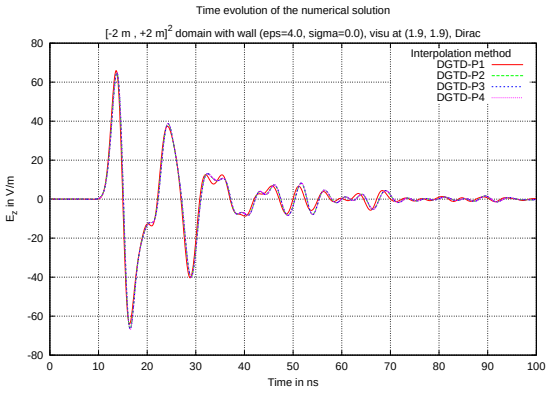

(c) Dirac source type

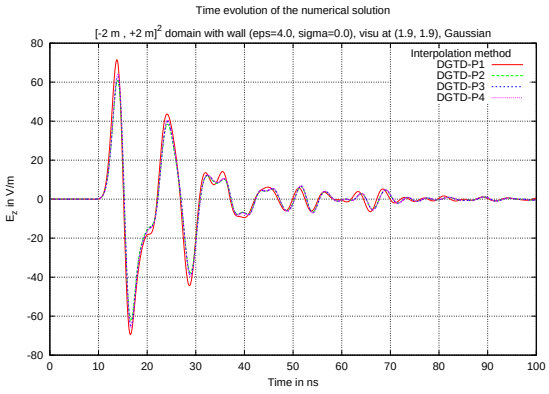

(d) Gaussian source type

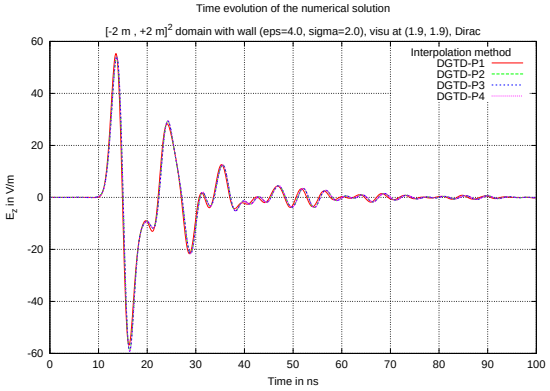

(e) Dirac source type

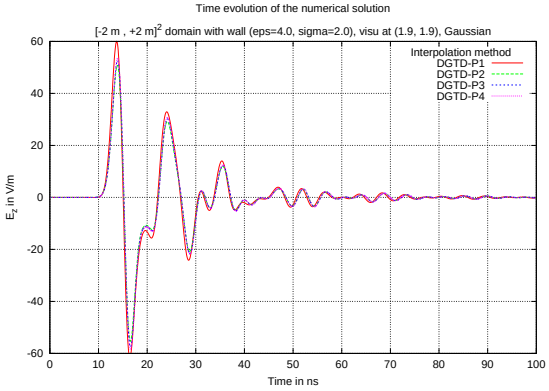

(f) Gaussian source type

Figure 15: Time evolution for the numerical solution in a $[-2m, +2m]^2$ domain with wall, meshed with about 1000 points

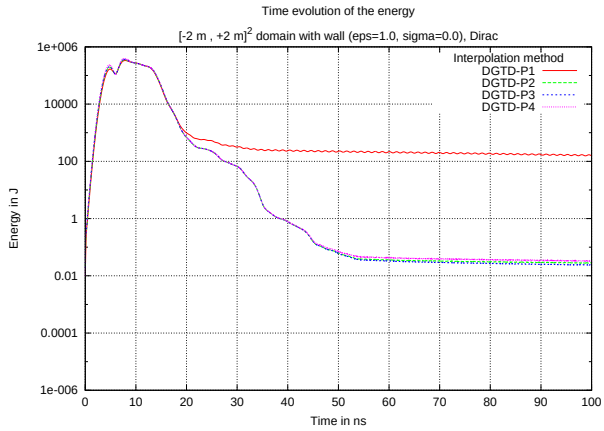

(a) Dirac source type

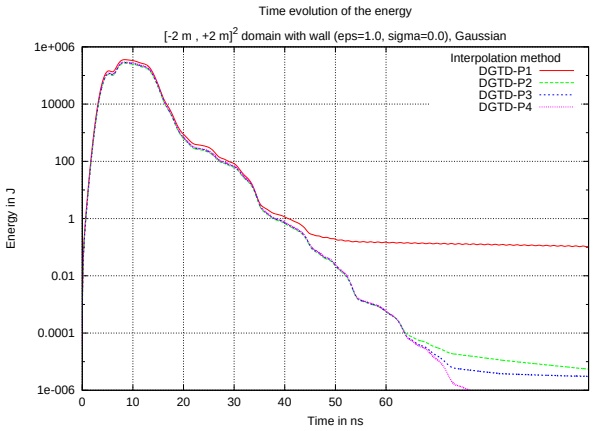

(b) Gaussian source type

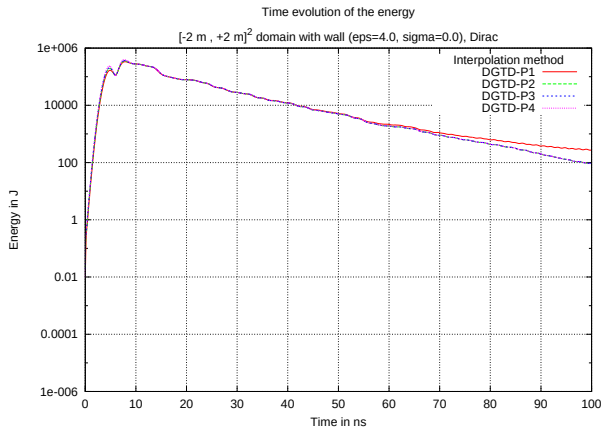

(c) Dirac source type

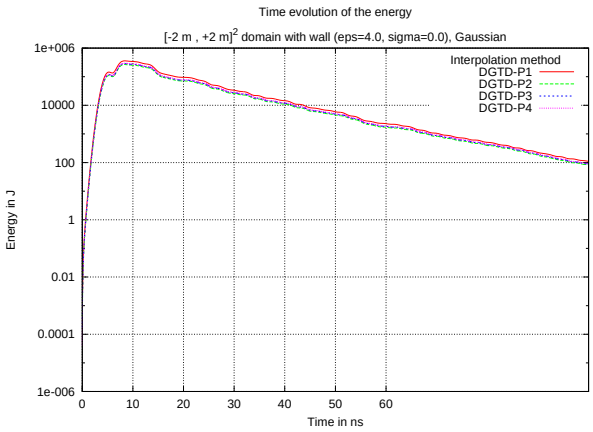

(d) Gaussian source type

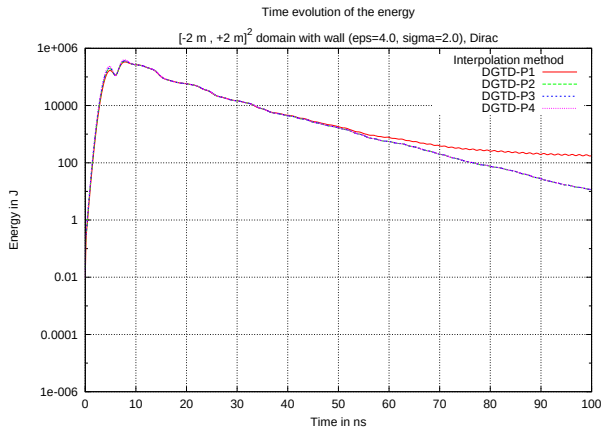

(e) Dirac source type

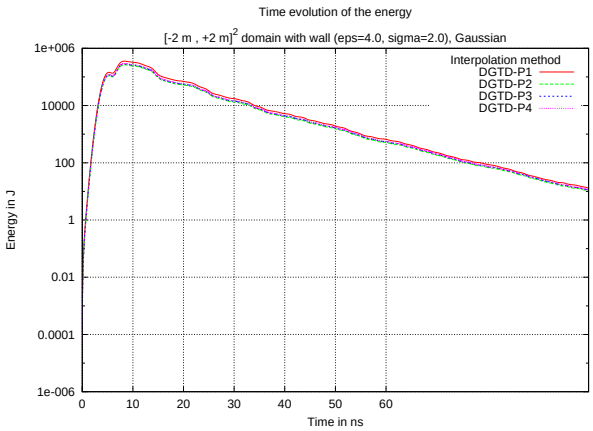

(f) Gaussian source type

Figure 16: Time evolution for the discrete energy in terms of the interpolation order in log scale

3.3.2 Influence of the size of the computational domain

Now we analyse the influence of the size of the domain. In Fig. 17 we observe again (see subsection 3.2.3) a time shift and a decrease of the absolute values of the amplitudes comparing Fig. 17 (b) and (c). On the other hand we analyse the observed signal at the same visualization point, changing the position of the absorbing boundary condition (Fig. 17 (a) and (b)). We see that these plots are very similar, so that at this point of the study we can focus on just one dimension of the domain (i.e. $[-2\,m, +2\,m]^2$).

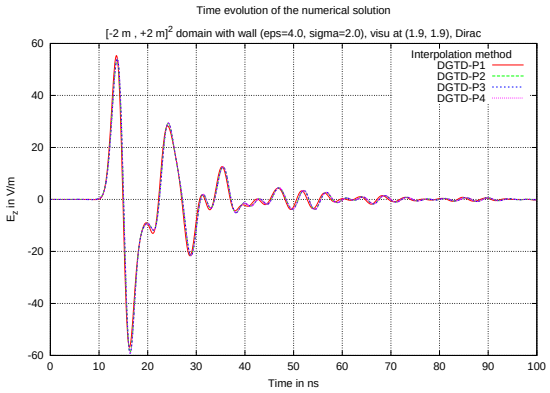

(a) meshed with about 1000 points

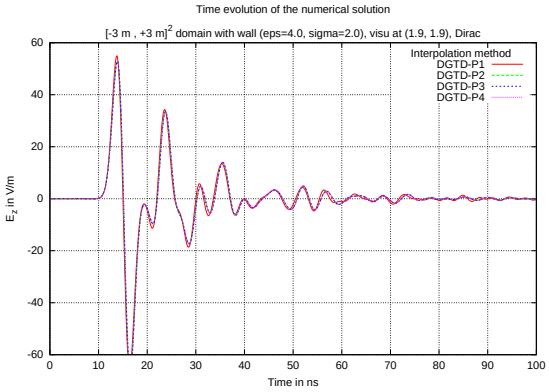

(b) meshed with about 1700 points

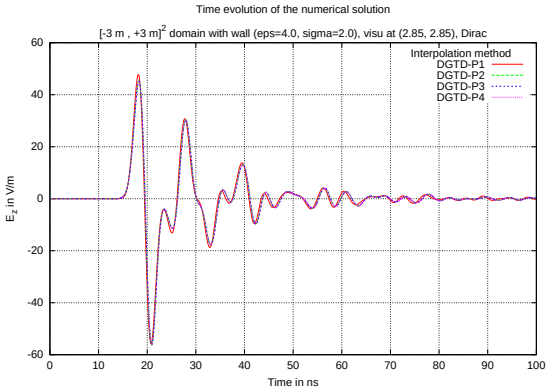

(c) meshed with about 1700 points

Figure 17: Time evolution for the numerical solution in a domain with wall (Dirac source type)

3.3.3 Influence of the position of the source

The radiating source so far was located at the center of the domain. Now it is moved outside the room and three visualization points are located behind the opposite wall so that the signal has to propagate through two walls. In Fig. 18 we observe two similar plots for the top left and top right visualization point with very low amplitudes while the top center visualization point has relativly high amplitudes. This propagation patterns might have the following two reasons. On the one hand the distance from the source to the top center visualization point less than the distance to the top left/right visualization point. On the other hand if we draw straight trajectories from the source to the visualization points we see that the part of the trajectories in the walls have different lengths which might have an impact on the amplitudes.

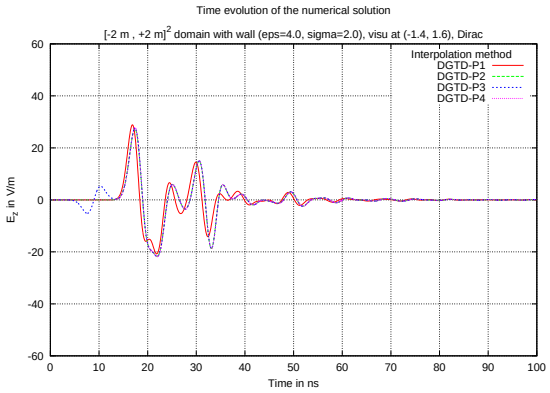

(a) top left

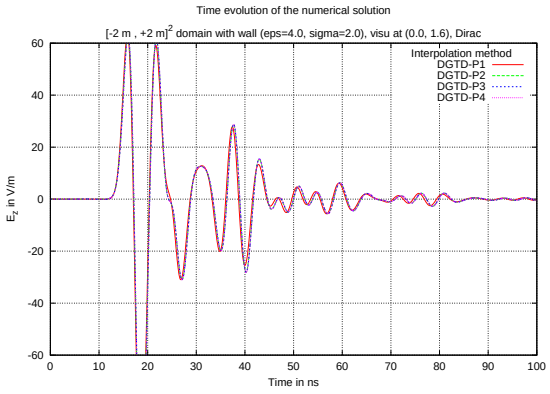

(b) top center

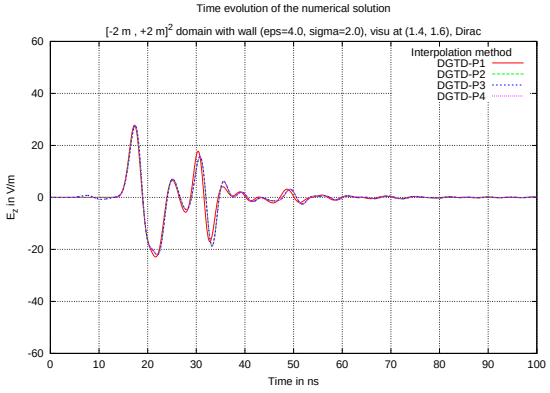

(c) top right

Figure 18: Time evolution for the numerical solution in a $[-2m, +2m]^2$ domain with wall, meshed with about 1000 points (moved Dirac source type)

3.4 Propagation involving objects inside the room

The meshes of the simulation settings are shown on Fig. 19. The radiating source is at first located at the center of the domain. Inside the room a circular object ($r = 20\,cm$) is modeled in the top right corner. In more detail there is either a metallic object or a meshed object with the parameters $\varepsilon = 8.0$ and $\sigma = 4.0$.

In Fig. 20 we have visualized the recieved signal at the top right visualization point, so the waves while propagating through the domain will pass the object. The metallic object has also transparent properties. In the zoomed plots we observe again that the solution converge very well for the DGTD-$\mathbb{P}_p$ with $p \geq 2$. We also observe higher amplitudes in the case of the meshed object.

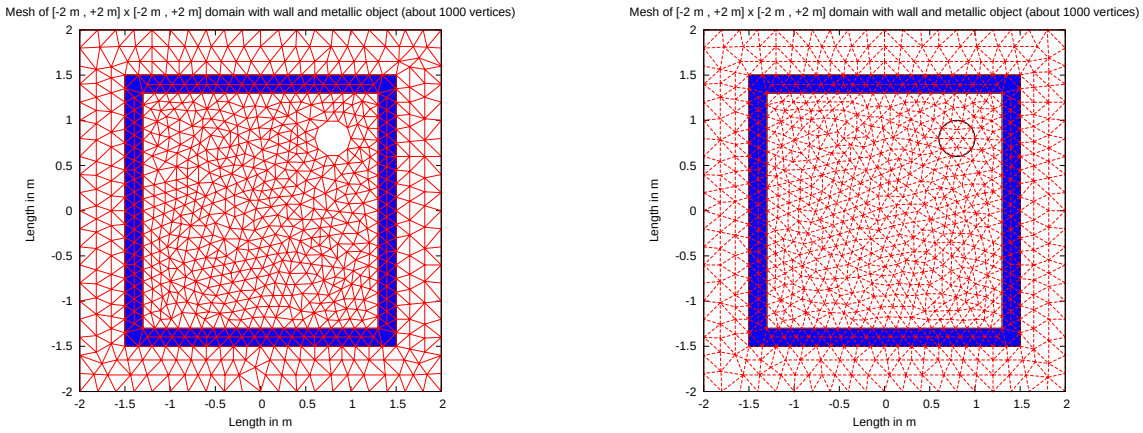

Figure 19: Problem setting for propagation involving objects inside the room

In Fig. 21 we have moved the source at the bottom center of the domain outside the room and observed behind the opposite walls (see subsection 3.3.3). We see very similar plots for the top left and top center visualization points, but observing the top right visualization point we do not have the symmetric pattern as in subsection 3.3.3 because of the objects inside.

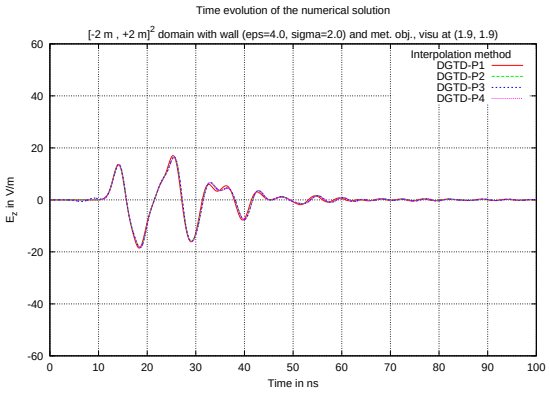

(a) metallic object

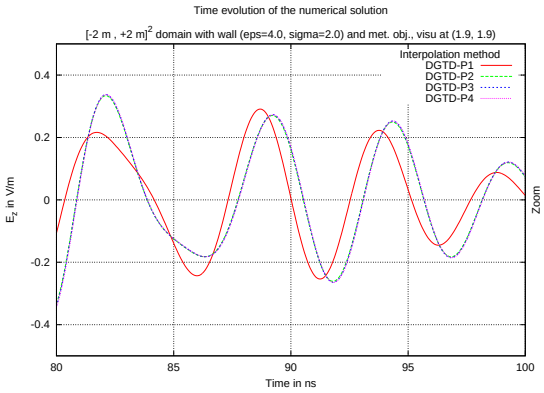

(b) metallic object

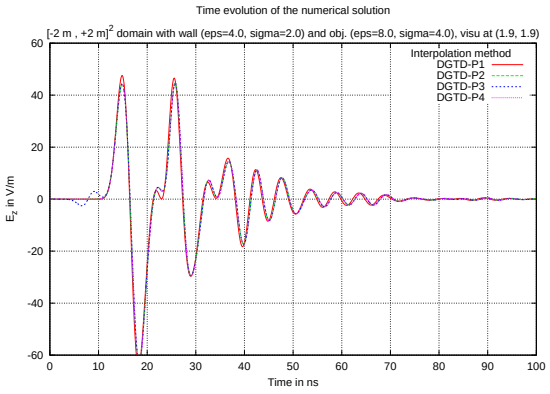

(c) meshed object

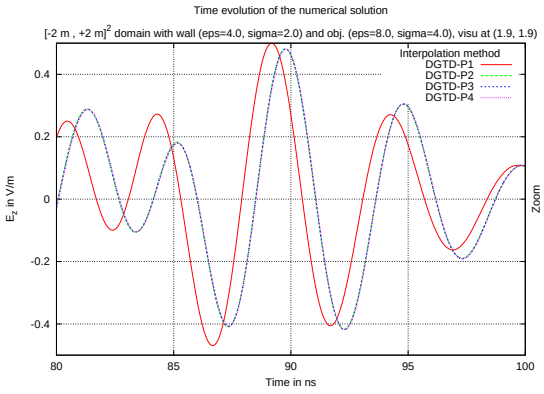

(d) meshed object

Figure 20: Time evolution for the numerical solution in a $[-2m, +2m]^2$ domain with wall and circular object inside the room, meshed with about 1000 points (Dirac source type)

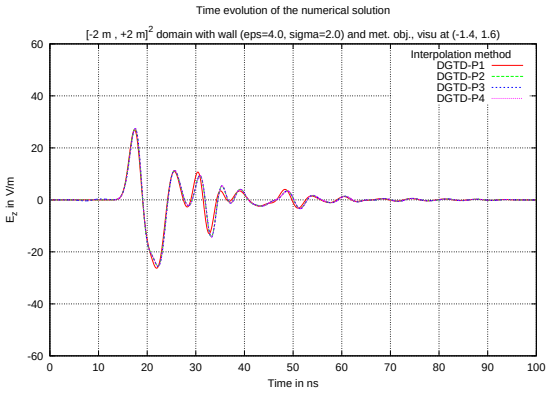

(a) metallic object

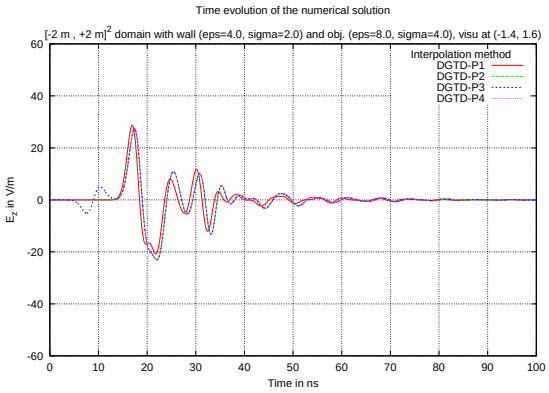

(b) meshed object

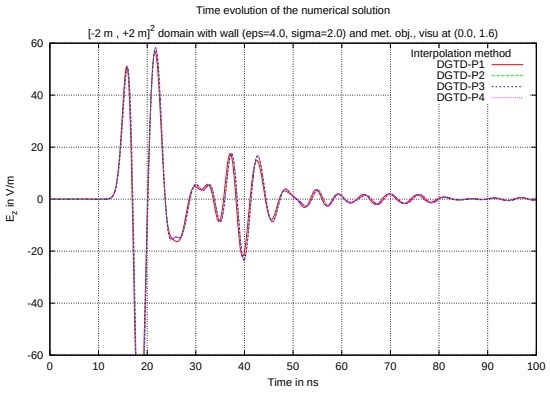

(c) metallic object

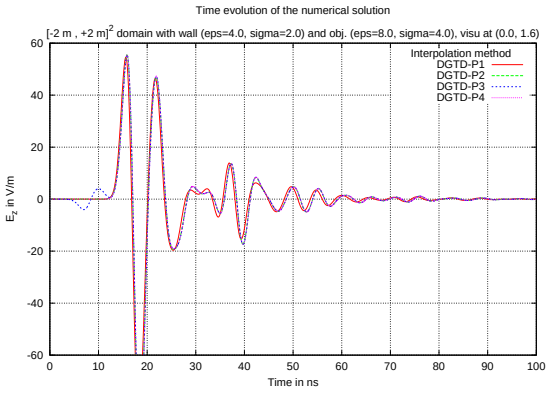

(d) meshed object

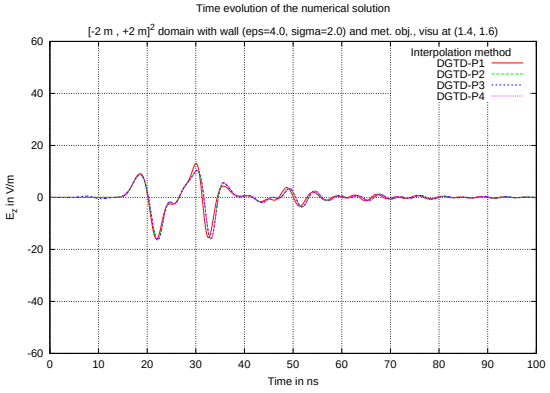

(e) metallic object

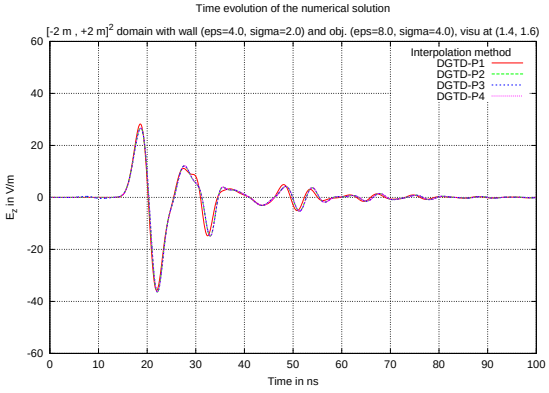

(f) meshed object

Figure 21: Time evolution for the numerical solution in a $[-2m, +2m]^2$ domain with wall and circular object inside the room, meshed with about 1000 points (moved Dirac source type)

4 Conclusions

In this study we have introduced the discontinuous Galerkin time domain method for the two-dimensional Maxwell equations with a radiating source term. Further on we used the implemented method and analysed the propagation patterns for different scenarios with increasing complexity numerically.

This study is a start for further numerical investigations of electromagnetic wave propagation generated by localized sources using a high order discontinuous Galerkin time domain method which will be continued by Jean-Yves Dauvignac from the Laboratoire d'Electronique, Antennes et Télécommunications, Stéphane Lanteri from the NACHOS project-team in INRIA and a PhD-Student. Because of the limited time we did not intend to have a very deep and detailed understanding of neither the discontinuous Galerkin time domain method, nor the Maxwell equations, nor the radiated signal analysis. We rather aimed to established a basis to work on for the PhD-Student. This included to test the existing code extensively on an easy grid in order to analyse the propagation pattern. Further tests on more difficult scenarios have been done with figures that might not be real physical quantities in order to see how the code works with numerical changes. We also established an efficient way to change the physical quantities and the configurations of the scenes as well as visualize the developped data after running a simulation and save it in a structured way.

The next steps are to analyse and interpret the plots in a more detailed way with a specialist for signal processing analysis. With those result there will be simulations using the real physical quantities (i.e. electric permittivity ε and and conductivity σ). Also there will be a number of simulations in order to assemble the weaknesses of the code as well as a profound understanding of the DGTD-$\mathbb{P}_p$ method. Then more complex configurations and meshes can be established and simulations can be runned in order to have a more detailed analysis of the propagation patern. I recall the overalll objective of this research is the development of a radar-based imaging system.

Acknowledgement

I personally liked it very much to be part of this research, the NACHOS project-team and INRIA. Now I have a deeper understanding of how it is like to work as a researcher. The people I was working with have been very friendly and welcoming. They had a very profound understanding of the topics and could answer all of my questions. Unfortunately I did not have access to the IT services of INRIA, so I had to adopt my laptop to another operating system environment which took a lot of time that I could not use for the given topic. On the other hand having experiences in different operating system is very valuable.

I wish the team all very best for the future as well as for the personal future of the team members. I also would like to express my special gratitude to my advisor Stéphane Lanteri.

References

[1] Bo Thidé, Electromagnetic Field Theory, Upsilon books, 2008.

[2] B. Cockburn, G. E. Karniadakis and C. W. Shu, editors, Discontinuous Galerkin methods. Theory, computation and applications, vol. 11 of Lecture Notes in Computational Science and Engineering, Springer-Verlag, 2000.

[3] L. Fezoui, S. Lanteri, S. Lohrengel and S. Piperno, Convergence and stability of a discontinuous Galerkin time-domain method for the heterogeneous Maxwell equations on unstructured meshes, ESAIM: Math. Model. and Numer. Anal., 39(2005), 1149–1176.

[4] J. S. Hesthaven and T. Warburton, Nodal Discontinuous Galerkin Methods, Springer, 54(2007)

[5] Wikipedia